agronomy

MDPI

Article

An Analysis of the Rice-Cultivation Dynamics in the Lower Utcubamba River Basin Using SAR and Optical Imagery in Google Earth Engine (GEE)

Angel James Medina Medina [1,2], Rolando Salas López [1], Jhon Antony Zabaleta Santisteban [1,2], Katerin Meliza Tuesta Trauco [1], Efrain Yury Turpo Cayo [3], Nixon Huaman Haro [1], Manuel Oliva Cruz [1,*] and Darwin Gómez Fernández [1,4]

[1] Instituto de Investigación para el Desarrollo Sustentable de Ceja de Selva (INDES_CES), Universidad Nacional Toribio Rodríguez de Mendoza (UNTRM), Chachapoyas 01001, Peru; angel.medina@untrm.edu.pe (A.J.M.M.); rsalas@indes-ces.edu.pe (R.S.L.); jhon.zabaleta@untrm.edu.pe (J.A.Z.S.); 7693686132@untrm.edu.pe (K.M.T.T.); nixon.huaman.epg@untrm.edu.pe (N.H.H.); darwin.gomez@untrm.edu.pe (D.G.F.)
[2] Programa de Maestría en Cambio Climático, Agricultura y Desarrollo Rural Sostenible, Escuela de Posgrado, Universidad Nacional Toribio Rodríguez de Mendoza de Amazonas, Chachapoyas 01001, Peru
[3] Programa de Doctorado en Recursos Hidricos (PDRH), Universidad Nacional Agraria La Molina, Ave. La Molina, S.N., Lima 15012, Peru; eturpo@lamolina.edu.pe
[4] Centro Experimental Yanayacu, Dirección de Supervisión y Monitoreo en las Estaciones Experimentales Agrarias, Instituto Nacional de Innovación Agraria (INIA), Carretera Jaén San Ignacio KM 23.7, Jaén 06801, Peru
* Correspondence: soliva@indes-ces.edu.pe; Tel.: +51-955-846-507

Abstract: One of the world's major agricultural crops is rice (Oryza sativa), a staple food for more than half of the global population. In this research, synthetic aperture radar (SAR) and optical images are used to analyze the monthly dynamics of this crop in the lower Utcubamba river basin, Peru. In addition, this study addresses the need to obtain accurate and timely information on the areas under cultivation in order to calculate their agricultural production. To achieve this, SAR sensor and Sentinel-2 optical remote sensing images were integrated using computer technology, and the monthly dynamics of the rice crops were analyzed through mapping and geometric calculation of the surveyed areas. An algorithm was developed on the Google Earth Engine (GEE) virtual platform for the classification of the Sentinel-1 and Sentinel-2 images and a combination of both, the result of which was improved in ArcGIS Pro software version 3.0.1 using a spatial filter to reduce the "salt and pepper" effect. A total of 168 SAR images and 96 optical images were obtained, corrected, and classified using machine learning algorithms, achieving a monthly average accuracy of 96.4% and 0.951 with respect to the overall accuracy (OA) and Kappa Index (KI), respectively, in the year 2019. For the year 2020, the monthly averages were 94.4% for the OA and 0.922 for the KI. Thus, optical and SAR data offer excellent integration to address the information gaps between them, are of great importance to obtaining more robust products, and can be applied to improving agricultural production planning and management.

Keywords: SAR; rice; monitoring; changes

Citation: Medina Medina, A.J.; Salas López, R.; Zabaleta Santisteban, J.A.; Tuesta Trauco, K.M.; Turpo Cayo, E.Y.; Huaman Haro, N.; Oliva Cruz, M.; Gómez Fernández, D. An Analysis of the Rice-Cultivation Dynamics in the Lower Utcubamba River Basin Using SAR and Optical Imagery in Google Earth Engine (GEE). *Agronomy* **2024**, *14*, 557. https://doi.org/10.3390/agronomy14030557

Academic Editor: Gniewko Niedbała

Received: 30 December 2023
Revised: 5 February 2024
Accepted: 16 February 2024
Published: 8 March 2024

1. Introduction

As one of the most vital crops globally, unhusked rice has had a significant impact not only on human society but also on the natural environment [1]. This cereal performs an essential role in subsistence [2], covering over 12 percent of the total cultivated land worldwide and providing sustenance to nearly half of the global population [3]. However, it is important to note that many farmers are modifying their agronomic practices, such as adopting new varieties and adjusting their water and fertilization management [4]. These

changes, in some cases, stem from policy decisions related to imports, exports, and prices, directly influencing the cultivation dynamics [5].

The acquisition of accurate and timely information about areas dedicated to cultivation is essential for calculating their agricultural production [6], establishing long-term development strategies, and making decisions aimed at ensuring food security [7]. Consequently, it is necessary to carry out precise and timely mapping and monitoring of rice crops as a prerequisite for effective agricultural management and to ensure food availability [8].

Therefore, it is crucial to have effective tools to monitor fluctuations in the extent of this crop [9]. In the last decade, there has been a rapid increase in the use of satellite-based remote sensing data to map and monitor rice fields [10]. However, the precise mapping of rice is primarily hindered by the frequent occurrence of clouds in such areas during the rice-cultivation season, significantly interfering with optical remote sensing observations [11]. For this reason, extensive research has been conducted in recent years on mapping and monitoring the expansion and reality of rice crops using synthetic aperture radar (SAR) information [4,12]. SAR data provide the opportunity to obtain information about crops without restrictions caused by weather and lighting conditions and with a spatial resolution of 1.5 m [13]. Time-series images, such as the data provided by Sentinel-1, are now available for free [10]; however, processing Sentinel-1 SAR data (time-series analysis) for crop monitoring can be a time-consuming task, and a cloud platform could streamline the process [8].

SAR technology, unlike optical images, has a high capability to capture and store images under cloudy conditions, light drizzle, and other meteorological phenomena [14]. Additionally, unlike optical imaging systems, SAR images are produced using microwave signals scattered back from the Earth's surface. Sentinel-1 SAR images, the first of the five in the Sentinel series under the European Copernicus program, provide free data. Sentinel-1 consists of the satellites Sentinel-1A and Sentinel-1B, which share the same orbital plane and capture images in the C-band (approximately a 5 cm wavelength) using SAR technology (an instrument called C-SAR). This results in a temporal resolution of 6 days for both satellites and 12 days for each. The C-SAR instrument operates at wavelengths unaffected by cloud cover or a lack of illumination, allowing data acquisition in areas of interest during the day or night and under all weather conditions [15].

In 2015, Google launched an environmental management and climate change-fighting tool called Google Earth Engine (GEE). This is a free platform that hosts petabytes of data spanning over 40 years of remote sensing data, including Landsat; MODIS; the Advanced Very High-Resolution Radiometer from the National Oceanic and Atmospheric Administration (NOAA AVHRR); Sentinels 1, 2, 3, and 5; and data from the Advanced Land Observing Satellite (ALOS). It is a cloud-based platform that enables the parallel processing of global-scale geospatial data using Google's cloud infrastructure [16]. GEE can be controlled using an internet-accessible Application Programming Interface (API) and an associated web-based Interactive Development Environment (IDE), allowing for rapid prototyping and visualization of the results [16].

Due to the flexibility of accessing GEE and the availability of the SAR images, there has been an increase in multitemporal analyses of water bodies [17,18] and land use changes, among other applications [19,20].

Examining changes in land cover, especially the expansion of rice cultivation, is crucial. Therefore, for this research, we propose classifying Sentinel-1 SAR images and Sentinel-2 optical images, jointly and by means of machine learning algorithms, based on the retrospective values for elements in the SAR images to analyze the monthly dynamics of land cover in the lower Utcubamba river basin. To achieve this, integration of these two sensors was performed, and large-scale image classification of the Sentinel-1 SAR and Sentinel-2 optical remote sensing images was successfully carried out using the GEE cloud computing technology. With this, we analyzed the monthly dynamics of rice cultivation by mapping and geometrically calculating the areas studied.

2. Materials and Methods

2.1. Study Area

The study area is situated between the departments of Amazonas and Cajamarca. Amazonas, where most of the study area is located, is in northwestern Peru, with an area of about 3,935,148.57 ha. The region is mostly covered by impenetrable tropical forests that remain unexplored [21], Amazonas comprises seven provinces and has a population of around 429,483 inhabitants [22]. The other portion in Cajamarca, also in northwest Peru, with an area of about 3,295,350.10 ha, consists of 13 provinces and has a population of approximately 1,454,217 inhabitants [22].

The study area includes zones in Bagua, Utcubamba, and Jaén provinces, as depicted in Figure 1. The prevailing climate in this region is "hot and dry" [23], with altitudes ranging from 400 to 1100 m above sea level.

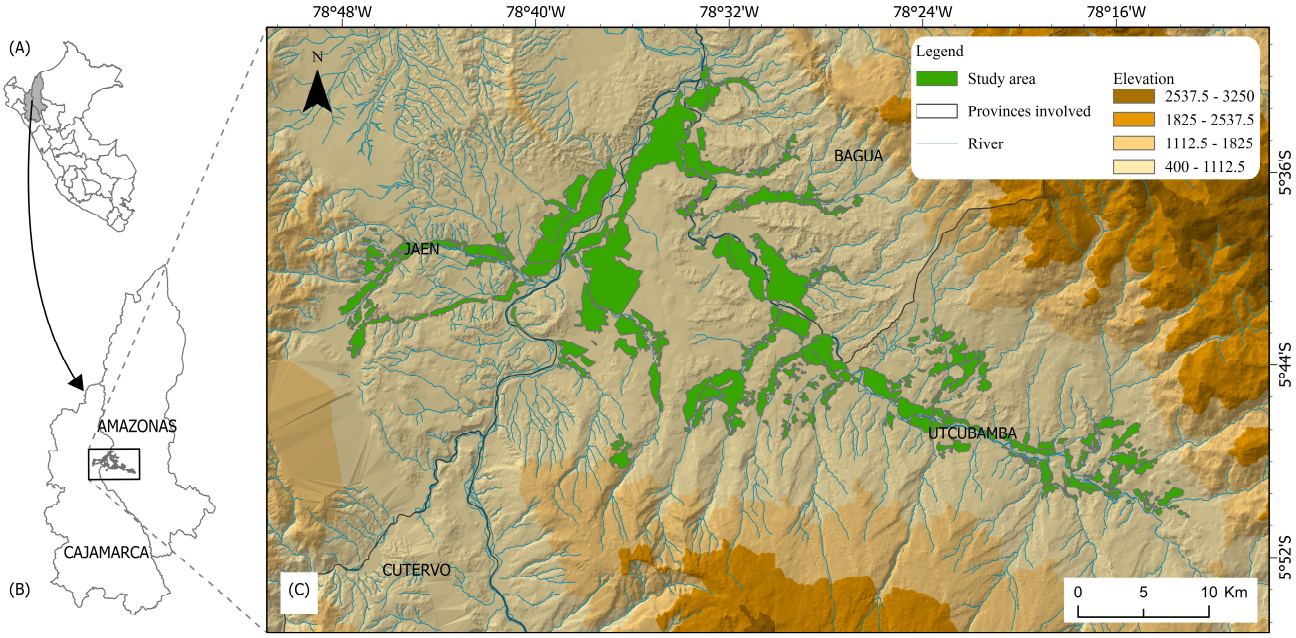

Figure 1. Location: (**A**) Republic of Peru, (**B**) Departments of Amazonas and Cajamarca, (**C**) Study area between the provinces of Jaén, Bagua, and Utcubamba.

2.2. Methodological Design

Figure 2 illustrates the flow chart used to determine the dynamics of rice cultivation in the lower Utcubamba river basin during 2019 and 2020 using images from the Sentinel-1 and Sentinel-2 missions on the GEE platform. The process started with a manual delimitation of the study area, followed by the introduction of SAR and Optical images, incorporation of auxiliary variables, speckle reduction, and inclusion of polygons for classification.

The classification was performed using Random Forest (RF) with Sentinel-1 only, Sentinel-2 only, and a combination of both, taking into account that this study assumes that these data are always available. The optimal classification was evaluated, resulting in the following maps. The classified images were processed in ArcGIS Pro; the minimum mapping unit considered for this study were areas larger than one hectare. Areas smaller than this were generalized to avoid overestimation and improve the visualization of each one; finally, the extent of growth and the stages of each month were determined. Principio del formulario.

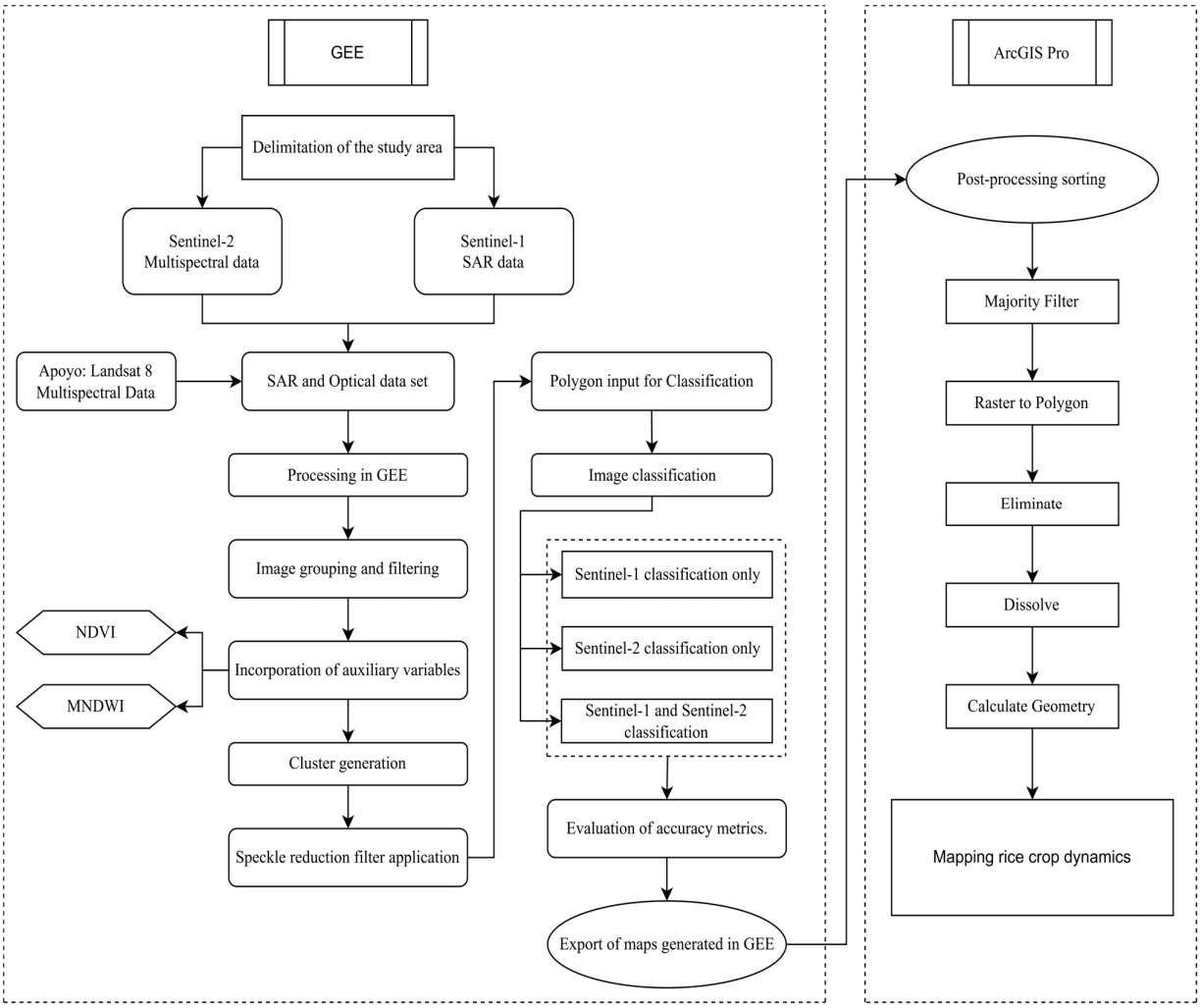

Figure 2. Methodological design.

2.3. Delimitation of the Study Area

The study area was manually delimited using Sentinel-2 optical imagery to mark the rice plots in 2019 and 2020. This procedure was carried out to avoid precision errors and confusion in the algorithm since the results may be affected in a subsequent evaluation analysis [24]. This procedure was executed in ArcGIS Pro software version 3.0.1.

2.4. Dataset

To obtain SAR data, Sentinel-1 images in Interferometric Wide-swath (IW) mode were used, which are available in GEE. The temporal resolution was 12 days, utilizing cross-polarization VH and VV, in addition to both Ascending (A) and Descending (D) flight directions [25], obtaining the combinations VHA, VVA, VHD, and VVD.

To obtain optical data in GEE, Sentinel-2 images were imported with a spatial resolution of 10 m. Additionally, for months when there was no availability and/or high cloud coverage, Landsat-8 images with a spatial resolution of 30 m were chosen.

2.5. Processing in GEE

Several studies have assessed land cover dynamics at various spatial scales, leveraging the capabilities of GEE. GEE provides access to data and advanced analytical techniques for big data. In the specific cartography of rice fields, both the research community and operators often utilize spatial information. Cloud-based platforms like GEE facilitate access to medium- and high-resolution satellite data, such as images from sensors including Multi

Spectral Instrument (MSI), Thematic Mapper (TM), Enhanced Thematic Mapper (ETM), and Operational Land Imager and Thermal Infrared Sensor (OLI.TIRS) [13]. The efficiency of the GEE platform is highlighted in executing complex workflows for processing satellite data required in large-scale applications, such as crop mapping [26]. We also made the code generated during the execution of this research available to promote the transparency and reproducibility of our results: https://code.earthengine.google.com/0811b809ed89944f6750cb197e8e5509 (accessed on 23 July 2023).

2.5.1. Image Grouping and Filtering

All available images from Sentinel-1, Sentinel-2, and Landsat 8 were grouped and filtered based on date ranges corresponding to the specific month under consideration. In this research, the results were analyzed on a monthly basis, covering individual months from January to December of 2019 and/or 2020.

2.5.2. Incorporation of Auxiliary Variables

Vegetation and water indices, based on reflectance data from each spectral band, were employed. Among various multispectral indices, the Normalized Difference Vegetation Index (NDVI) [27] is commonly used to monitor vegetation health, land use planning, and ecosystem monitoring [28].

Additionally, the Modified Normalized Difference Water Index (MNDWI) [29–31], known for its effectiveness in delineating water and providing a relatively constant threshold compared to other water indices, was applied [32]. It is considered the most accurate available [33] and was selected as a feature for contour extraction in water bodies [34]. Table 1 details the formulas for the aforementioned indices.

Table 1. Spectral indices used as auxiliary variables.

Index	Description	Formula	Source
NDVI	Normalized Difference Vegetation Index	$\text{NDVI} = \left(\frac{NIR-RED}{NIR+\text{RED}}\right)$	[27]
MNDWI	Modified Normalized Difference Water Index	$\text{MNDWI} = \frac{\rho Green-\rho SWIR}{\rho Green+\rho SWIR}$	[31]

2.5.3. Cluster Generation

The purpose of cluster analysis is to group data based on their similarity [35]. To achieve this, the algorithm automatically normalizes the input numerical attributes and employs Euclidean distance to measure distances between groups, aiming to minimize the variation (distances) within the groups [10]. In this research, the GEE platform "*ee.Algorithms.Image.Segmentation.SNIC*" was utilized to generate the respective clusters.

2.5.4. Speckle Reduction Filter Application

The noise present in images, commonly known as speckle, is generated during the SAR image-generation process and has a significant impact on image quality and target-extraction capabilities [36]. One strategy to reduce this speckle involves multitemporal stack aggregation, allowing reduction without compromising spatial resolution. This approach contrasts with the more common speckle-filtering practice, which involves comparing neighboring pixels in a single-date image and often results in a loss of spatial resolution [37]. Therefore, the GEE platform function "*ee.Image.focal_median*" was used for speckle reduction to enhance and refine the image quality of Sentinel-1.

2.5.5. Image Classification

Prior to classification, training samples (polygons) were utilized to generate monthly maps placed in distinct zones representing various stages of rice cultivation. For the purposes of this research, they were separated into 4 major groups.

The first stage is referred to as "Stage 1" (flooded areas), the second stage is referred to as "Stage 2" (areas with rice cultivation one to two months old), the third stage is referred to as "Stage 3" (areas with mature rice cultivation), and finally, the fourth stage is named "Stage 4" (areas covered with rice fields ready to be harvested).

Subsequently, it was decided to use the Random Forest (RF) classifier in a pixel-based classification to categorize the selected images [38]. The RF, a nonparametric machine learning classifier, was used for the task of land cover classification by visual or digital interpretation [39].

For this research, three data groups were classified: the first ones resulting from the Sentinel-1 mission (SAR data), the second comprising optical data from Sentinel-2 and/or Landsat 8 based on availability, and finally, the third group consisting of the combination of SAR and Optical data.

2.5.6. Evaluation of Accuracy Metrics

In order to measure the accuracy of the classification results and provide a comprehensive assessment of the algorithm's performance, we calculated two common statistical indicators that offer precision metrics for Land Use and Land Cover (LULC) maps [40]. These indicators are Overall Accuracy (OA) and Kappa Index (KI).

2.5.7. Export of Maps Generated in GEE

Finally, the maps for all processed months were exported in Geotiff format. Firstly, they were exported as "LULC," a dataset that provided information on land distribution and use, i.e., the various rice coverages. Secondly, they were exported as bands of the visible light spectrum, a dataset that, when combined, produces a visual representation similar to what we would see with the naked eye from space. The combination of both formats aided in the visual analysis conducted in the post-classification phase.

2.6. Post-Processing Sorting

The products generated in GEE were imported into ArcGIS Pro version 3.0.1 software in order to improve the quality of each monthly map; a spatial filter was applied to reduce the pepper salt effect (areas smaller than one hectare was generalized), and the calculation of areas for each rice stage evaluated was performed. For this purpose, toolbox functions were used, such as Majority Filter, Raster to Polygon, Eliminate, Dissolve, and Calculate Geometry.

2.7. Shapiro–Wilk Test

A comparison between the years 2019 and 2020 was carried out with the objective of identifying statistical differences. To establish the normality of the data, the Shapiro–Wilk test was applied, using the null hypothesis (H0) with a p-value < 0.05, indicating that the sample follows a normal distribution, and the alternative hypothesis (H1) with a p-value > 0.05 that contradicts the normality of the data [41].

Subsequently, a t-test for paired samples was performed, where H0 is accepted if the p-value > 0.05, indicating that the mean value of the years is equal, and H1 is accepted if the p-value < 0.05, suggesting that the mean values of the years are different. All this was performed in R 3.3.0 software, using the ggplot 2 library [41].

3. Results

3.1. Distribution and Availability of Data

Figure 3 details the monthly distribution and availability of SAR and Optical data used in this study. It can be observed that, generally, a greater amount of SAR data can be obtained from the GEE platform. In total, 79 and 89 SAR images were obtained for the years 2019 and 2020, respectively. Similarly, 52 and 44 Optical images were acquired for the years 2019 and 2020, respectively.

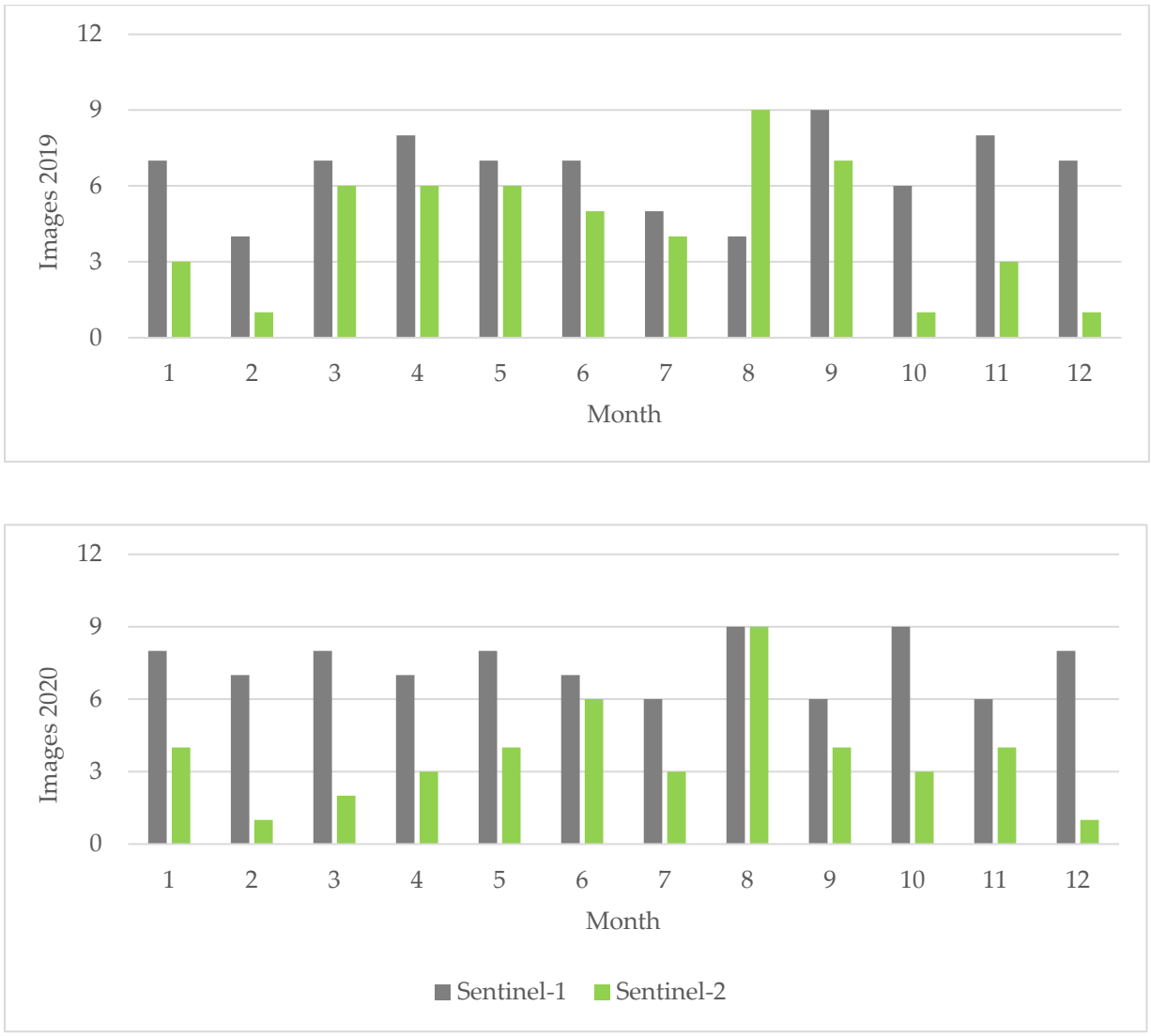

Figure 3. SAR and Optical images available for 2019 and 2020.

3.2. Accuracy Metrics and LULC Maps

For the year 2019, as seen in Figure 4, the classification using Sentinel-1 data for the OA metric obtained the lowest accuracy value in the month of February, with a precision of 70.99%, and the highest accuracy in January, with a precision of 94.27%. Regarding the KI metric, the lowest accuracy was achieved in August, with a value of 0.6147, and the highest accuracy was attained in January, with a precision of 0.9191.

Similarly, the classification using only Sentinel-2 data for the OA metric obtained the lowest accuracy value in the month of July, with a precision of 73.02%, and the highest accuracy in May, with a precision of 97.72%. Regarding the KI metric, the lowest accuracy was achieved in July, with a value of 0.6420, and the highest accuracy was attained in May, with a precision of 0.9676.

Finally, the classification using the combination of Sentinel-1 and Sentinel-2 data for the OA metric obtained the lowest accuracy value in the month of November, with a precision of 90.51%, and the highest accuracy in March, with a precision of 100%. Regarding the KI metric, the lowest accuracy was achieved in November, with a value of 0.8720, and the highest accuracy was attained in March, with a precision of 1.

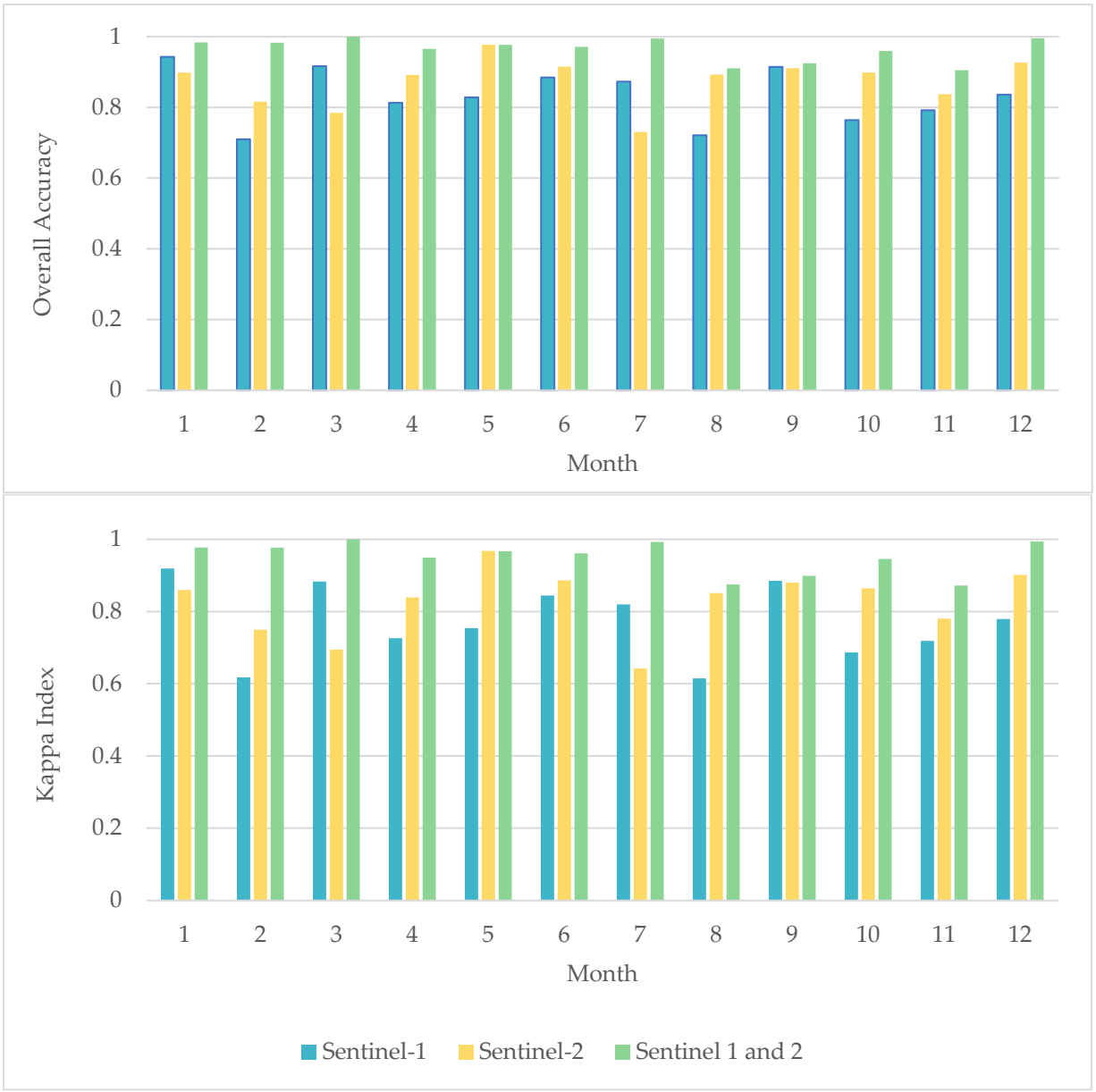

Figure 4. Accuracy metrics for 2019 for Sentinel-1 only, Sentinel-2 only, and combined Sentinel-1 and Sentinel-2 classifications.

Similarly, for the year 2020, as shown in Figure 5, the classification using only Sentinel-1 data for the OA metric obtained the lowest accuracy value in the month of October, with a precision of 65.67%, and the highest accuracy in January, with a precision of 90.72%. Regarding the KI metric, the lowest accuracy was achieved in February, with a value of 0.6295, and the highest accuracy was attained in January, with a precision of 0.8716.

Similarly, the classification using only Sentinel-2 data for the OA metric obtained the lowest accuracy value in the month of December, with a precision of 68.71%, and the highest accuracy in June, with a precision of 95.63%. Regarding the KI metric, the lowest accuracy was achieved in December, with a value of 0.5810, and the highest accuracy was attained in June, with a precision of 0.9359.

Finally, the classification using the combination of Sentinel-1 and Sentinel-2 data for the OA metric obtained the lowest accuracy value in the month of October, with a precision of 89.47%, and the highest accuracy in January, with a precision of 98.40%. Regarding the KI metric, the lowest accuracy was achieved in October, with a value of 0.8523, and the highest accuracy was attained in January, with a precision of 0.9780.

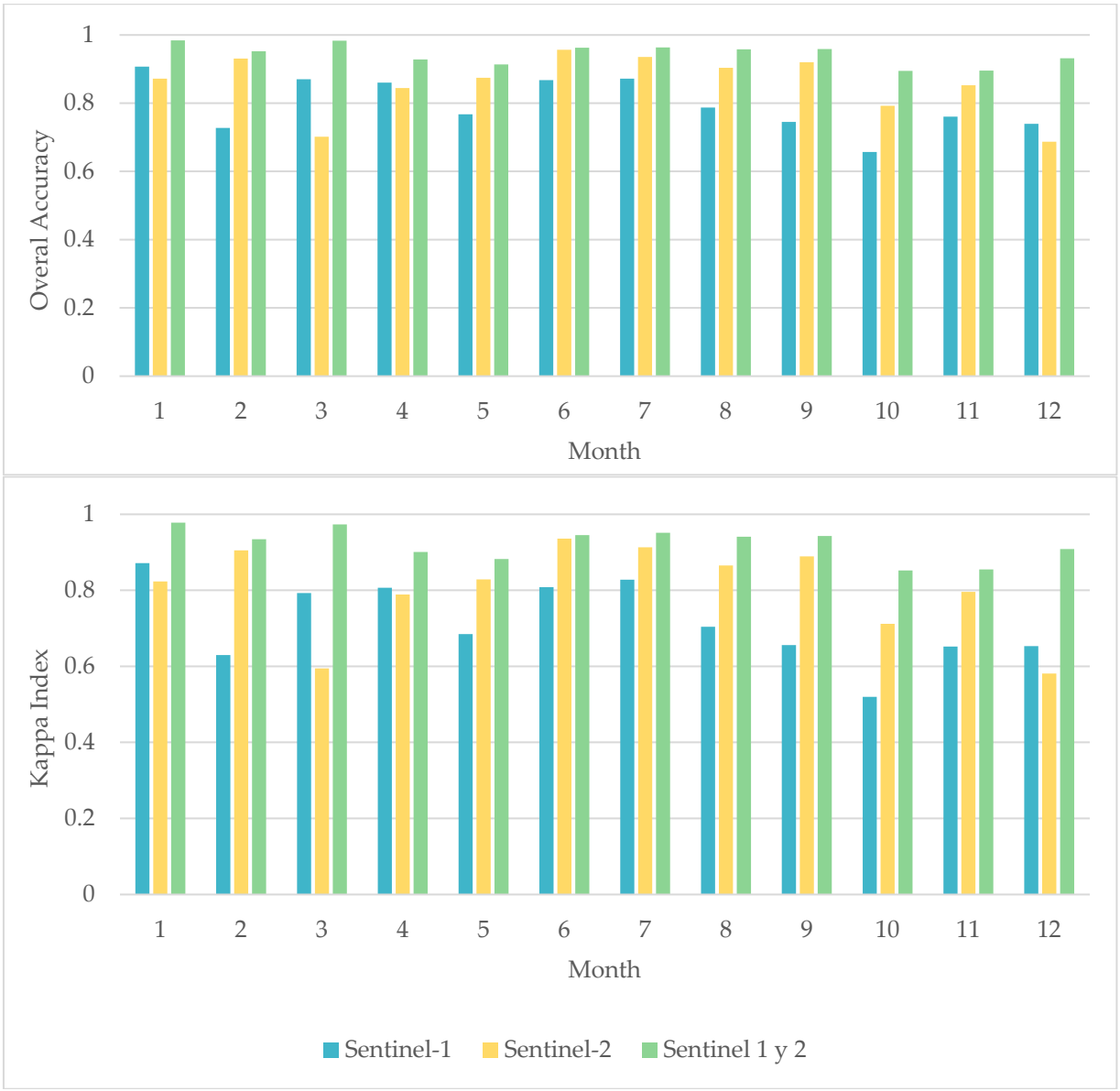

Figure 5. 2020 accuracy metrics for the Sentinel-1 only, Sentinel-2 only, and combined Sentinel-1 and Sentinel-2 classifications.

In this regard, the best classification for the export of LULC maps was selected. For all months, the classifications of the combination of Sentinel-1 and Sentinel-2 images were chosen since they generally achieved higher accuracy for both calculated metrics. Table 2 details the average accuracy values for both years and all three classifications. The best classifications were obtained in the combination of Sentinel-1 and Sentinel-2, with an OA of 96.4% and KI of 0.951 for the year 2019 and an OA of 94.4% and KI of 0.922 for the year 2020.

Table 2. Overall average accuracy metrics for both years.

	Sentinel-1		**Sentinel-2**		**Sentinel 1 and 2**	
Year	OA	KI	OA	KI	OA	KI
2019	83.3%	0.771	87.3%	0.826	96.4%	0.951
2020	79.7%	0.717	85.6%	0.803	94.4%	0.922

3.3. Mapping of Classified Rice Areas

Figures 6 and 7 display classified maps of rice areas for every month in the years 2019 and 2020, created from the combination of SAR and Optical images, showcasing the four stages (stage 1, stage 2, stage 3, and stage 4).

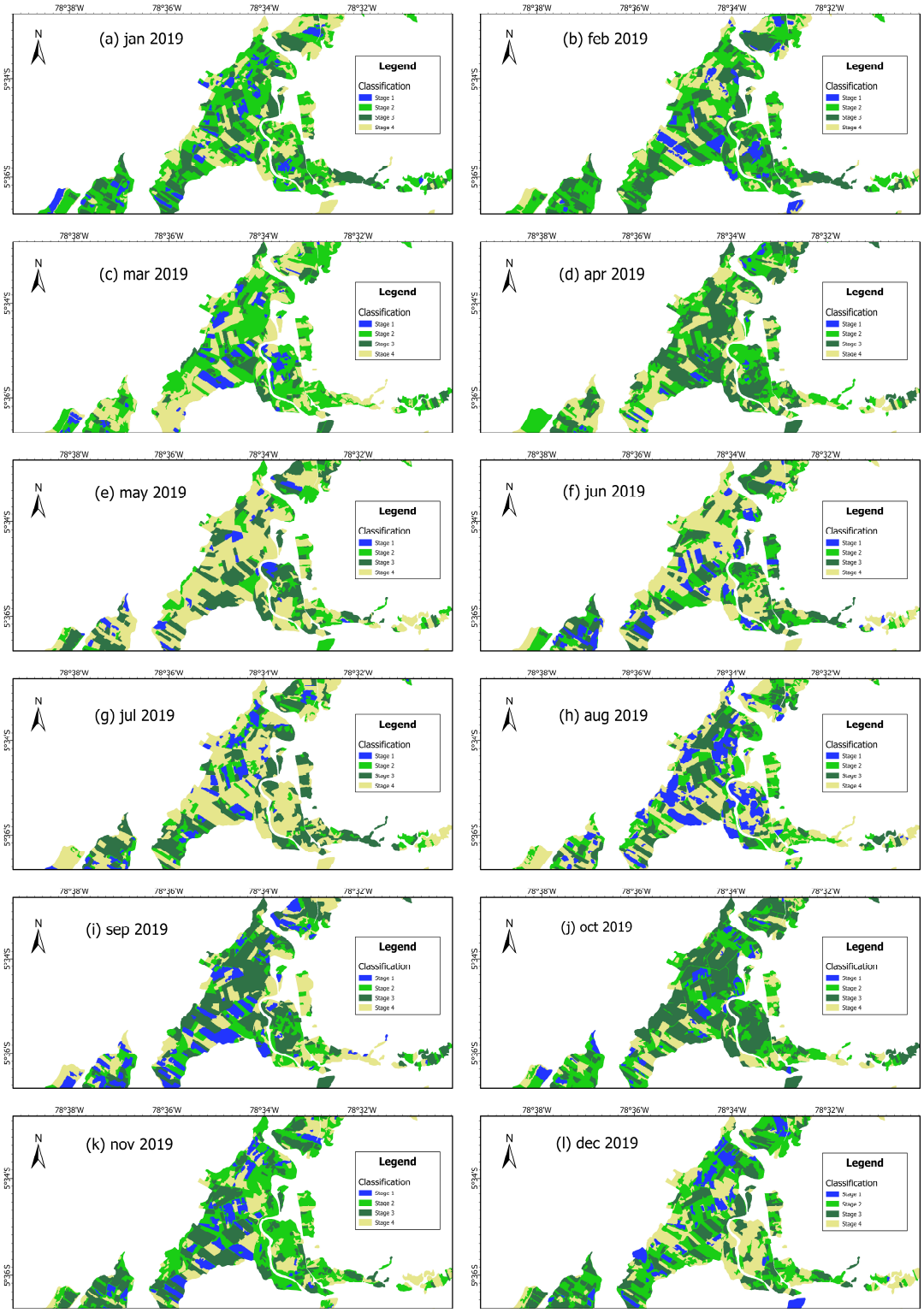

Figure 6. Mapping of rice areas, from January to December 2019.

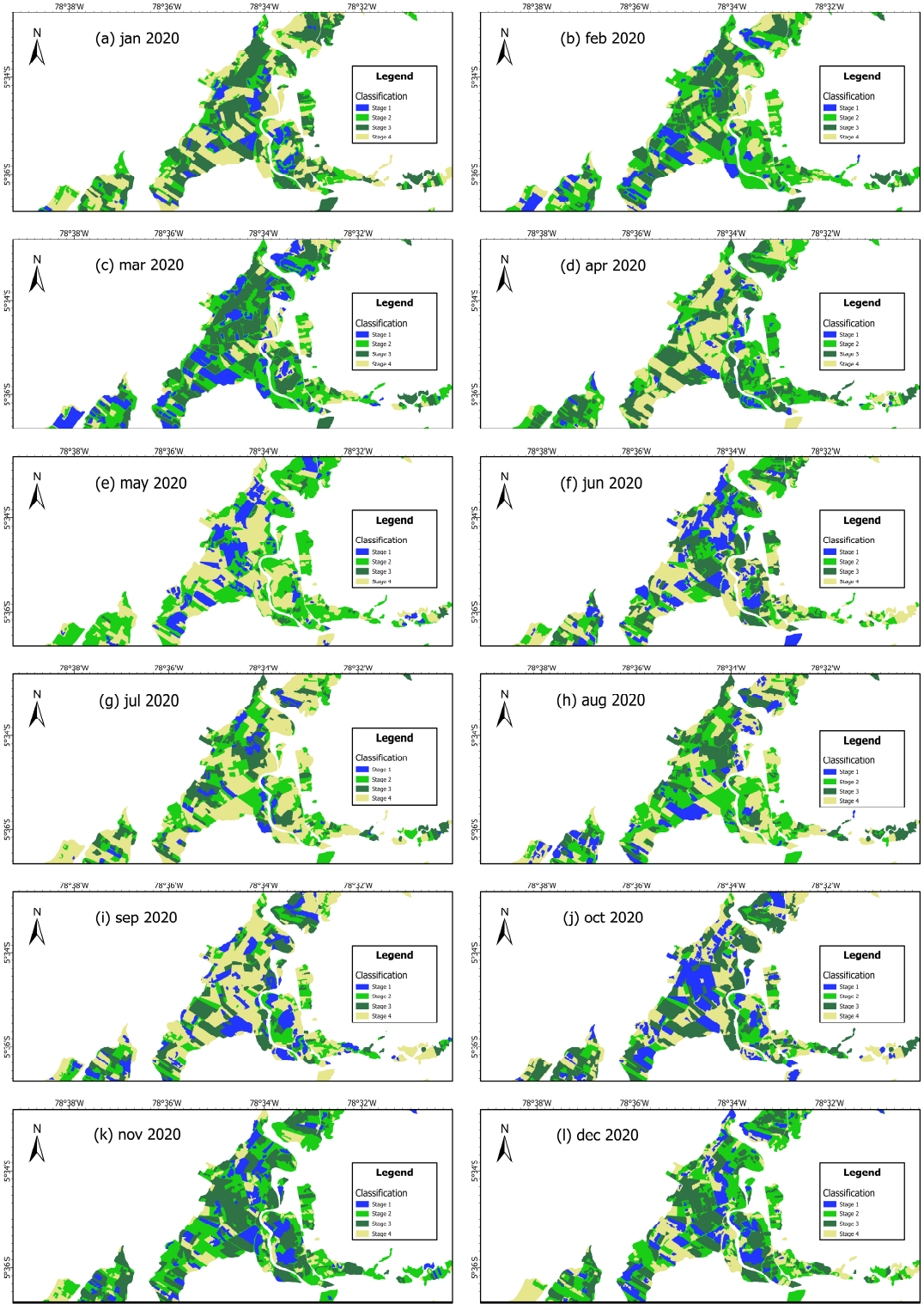

Figure 7. Mapping of rice areas, from January to December 2020.

3.4. Geometric Attributes

Figure 8 depicts the variation in areas (hectares) resulting from the combination of SAR and Optical images for Stage 1, Stage 2, Stage 3, and Stage 4. It can be observed that for water-covered areas, there is no abrupt monthly change compared to the other stages. For Stage 2, there is a significant monthly variation, with March 2019 and February 2020 registering the highest changes. This suggests that the majority of newly planted areas are

typically cultivated in the first quarter of each calendar year. For the phenological stage of harvest (Stage 4) in rice cultivation, it is observed that producers typically harvest their plots during the months of July to December for both years.

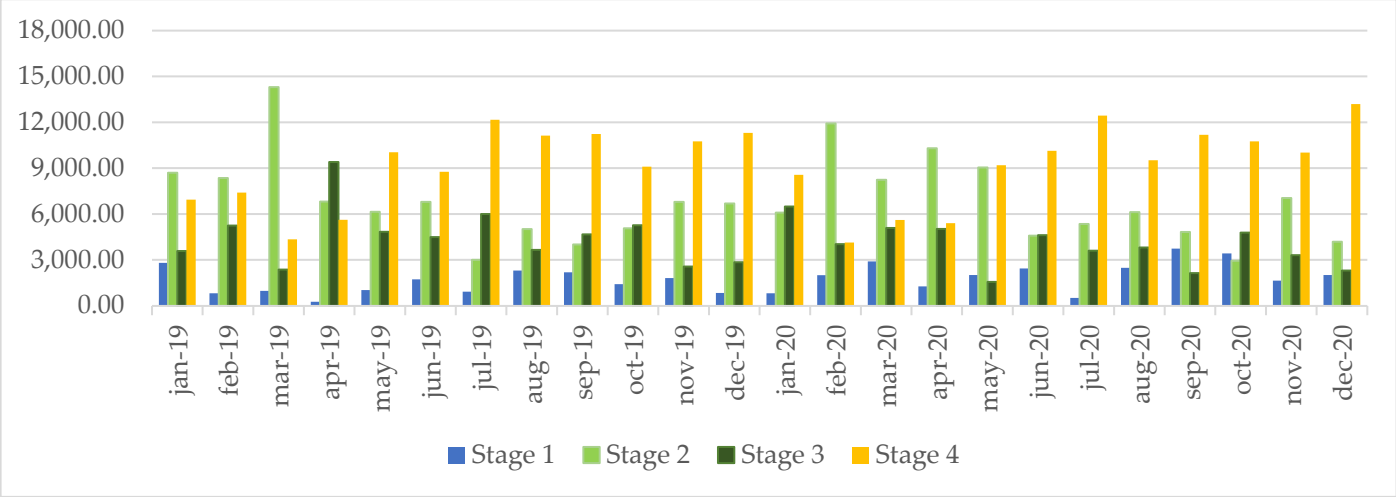

Figure 8. Area variation in hectares for Stage 1, Stage 2, Stage 3, and Stage 4.

Table 3 presents the overall summary for each studied year. Concerning harvest values, it can be observed that there is no significant variation between the two years, with a total of 108,800.401 hectares for the year 2019 and 110,127.272 hectares for the year 2020.

Table 3. Estimated area (ha) for the years 2019 and 2020.

	2019	**2020**
Stage 1	17,089.974	25,243.385
Stage 2	81,691.886	80,662.511
Stage 3	54,911.457	46,749.004
Stage 4	108,800.401	110,127.272

3.5. Shapiro–Wilk Test

Table 4 shows the results of the Shapiro–Wilk test for the years 2019 and 2020, which evaluates the normality of the data. For the year 2019, a *p*-value of 0.05646 is obtained, slightly higher than the significance level of 0.05, which indicates that the null hypothesis that the distribution of the data is normal is accepted. Similarly, for the year 2020, the *p*-value is 0.005821, which is less than 0.05, indicating that the data also have normality for that year.

Table 4. Shapiro–Wilk test.

Shapiro–Wilk Normality Test	
Year 2019	Year 2020
data: df_19$Value	data: df_20$Value
W = 0.95375, *p*-value = 0.05646	W = 0.92813, *p*-value = 0.005821

In Table 5, given the high *p*-value and the confidence interval that includes 1, the null hypothesis cannot be rejected. Therefore, the variance of both years is significantly equal.

Table 5. F test to compare two variances.

F Test to Compare Two Variances			
data:	df_19$Value and df_20$Value		
F = 1.0729	num df = 47	denom df = 47	*p*-value = 0.8104
alternative hypothesis:	true ratio of variances is not equal to 1		
95 percent confidence interval:	Upper Limit	Lower limit	
sample estimates:	0.6014441	1.913864	
ratio of variances	1.072885		

Figure 9 displays the statistical difference between the "Stages" in the years 2019 and 2020, with the hectares on the x-axis and the *p*-values on the y-axis. It is observed that the statistical difference is minimal for each stage and year, which suggests a normal distribution of the data.

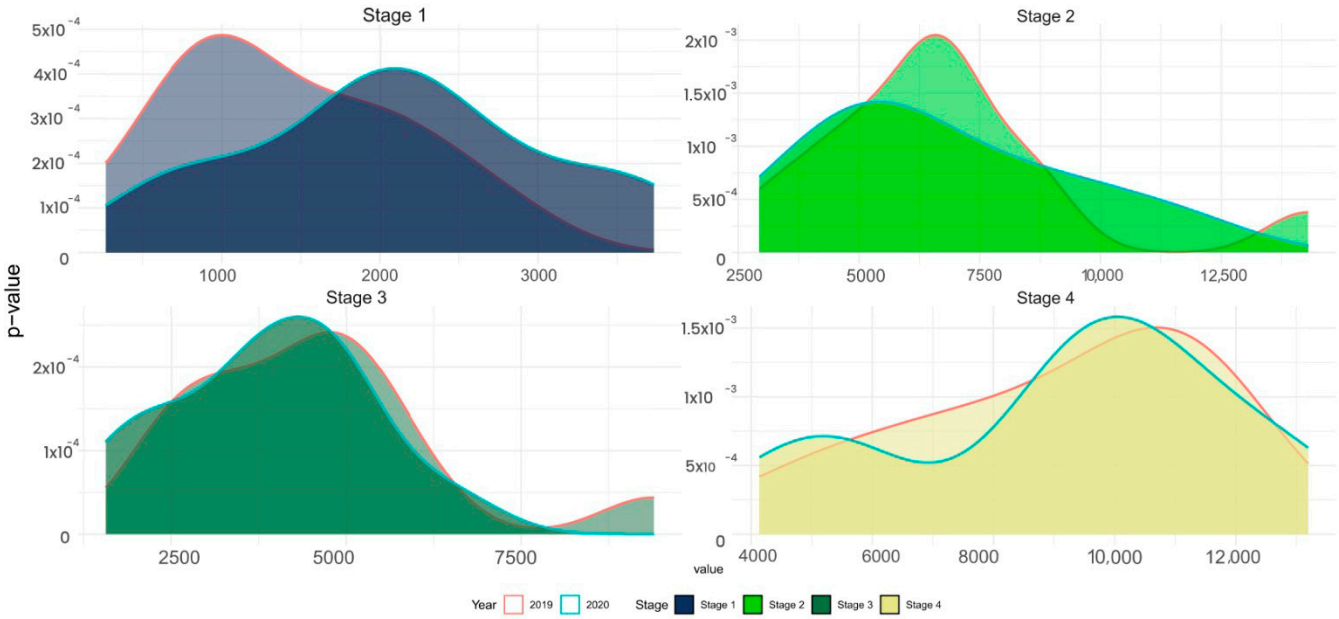

Figure 9. Statistical difference between the "Stages" in 2019 and 2020.

4. Discussion

Obtaining accurate and timely crop data on a global scale is crucial for ensuring food security and sustainable development. The use of satellites for remote sensing provides an economical monitoring alternative compared to the conventional method of on-site inspection, which requires expensive human resources and consumes a significant amount of time [42].

This study emphasizes the importance of combining data from Optical and SAR images through the multifunctional platform of GEE during the growth phases of rice cultivation (i.e., vegetative, reproductive, and maturation). However, previous studies [28,43] developed vegetation and farmland monitoring methods using remote sensing, relying solely on Optical images such as Landsat and Sentinel-2 databases. Similarly, other research [4,7,13,44,45] has employed Sentinel-1 time series (SAR data), primarily for mapping and monitoring rice crop stands, identifying land use and cover, and identifying water coverage. This improved the validation and suitability of the results, demonstrating a positive correlation in crop yield prediction.

In recent years, there have been successful efforts to integrate various datasets, such as Landsat, Sentinel-1, Sentinel-2, and PlanetScope (PL) [42,46–49]; the latter has become

available more recently on the GEE platform [16]. This combination produces more robust results compared to using a single data source, and it generally achieves higher accuracy. For example, a study by [50] classified a highly diverse agricultural region for 2020 and 2021, achieving accuracies of 95.2%. That research study concluded that integrating both satellite datasets enhanced overall accuracy by 2.94%.

In this research, integrated data from Sentinel-1 and Sentinel-2 were used to classify rice-cultivation dynamics, and this combination yielded the best results in terms of accuracy, as measured by OA and KI metrics. The highest precision results for both years were between 97.8% and 100%. This is similar to the findings of [50], who concluded that the combination of Sentinel-1 and Sentinel-2 data enables accurate early mapping of crops in the studied area, achieving an OA of up to 95.02%.

The scenarios reveal that the monthly temporal series offers superior performance in terms of classification accuracy compared to individual images within monthly windows. Similarly, ref. [40], through a comparative analysis, determined that achieving precise mapping of crop types at a regional level involves using a combination of multiple images with single-moment characteristics and images derived from temporal series of Sentinel-1 and Sentinel-2, resulting in outstanding performance.

This approach enables precise mapping of various crop types with a resolution of 10 m for extensive areas. The OA and Kappa Coefficient (KC) turned out to be 84.15% and 0.80, respectively. Another example is the research by Vizzari [42], which aimed to evaluate the advantages of land cover classification by integrating PlanetScope (PL) datasets with Sentinel-2 and Sentinel-1 data. The integration of PL data with S2 and S1 datasets improved overall accuracy results for PB and OB (82 versus 67% and 91 versus 82%, respectively).

5. Conclusions

This research confirmed that Optical and SAR data offer excellent integration to address information gaps between them and are of great importance to obtaining more robust products. Unfortunately, classification methods using only Sentinel-1 SAR data are challenging to handle. Therefore, it is necessary to work by combining them with optical data from Sentinel-2 or Landsat 8 to achieve better results. This combination was conducted on a monthly and metric basis to ensure a sufficient amount of updated data without interference from clouds. A total of 79 SAR images were obtained in 2019 and 89 in 2020; likewise, the quantity of optical images was 52 in 2019 and 44 in 2020. It is worth noting that a semi-automatic methodology was applied to process optical and SAR images using the GEE platform for the years 2019 and 2020 in the provinces of Utcubamba, Bagua, and Jaén.

The spatial dynamics of rice cultivation were successfully determined, achieving an average monthly precision of 96.4% and 0.951 for OA and KI, respectively, in the year 2019. For the year 2020, the monthly averages were 94.4% for OA and 0.922 for KI. In another way, the harvest results were 108,800.401 hectares for the year 2019 and 110,127.272 hectares for the year 2020. This indicates and reaffirms that, during the first year of the pandemic (2020), producers and the cultivated lands of basic food items in the Peruvian family basket were crucial for survival, as they continued their activities without interruptions. Finally, the proposed approach is accurate and cost-effective, as the data on the platforms used are open source and freely available.

Author Contributions: Conceptualization, A.J.M.M. and D.G.F.; Data curation, A.J.M.M., E.Y.T.C., R.S.L., N.H.H. and J.A.Z.S.; Formal analysis, A.J.M.M., D.G.F. and E.Y.T.C.; Investigation, A.J.M.M., R.S.L., J.A.Z.S., K.M.T.T., E.Y.T.C., N.H.H., M.O.C. and D.G.F.; Methodology, A.J.M.M., R.S.L., J.A.Z.S., K.M.T.T., E.Y.T.C., N.H.H., M.O.C. and D.G.F.; Project administration, R.S.L. and M.O.C.; Resources, R.S.L. and M.O.C.; Software, A.J.M.M., R.S.L., E.Y.T.C. and D.G.F.; Supervision, R.S.L.; Validation, K.M.T.T. and N.H.H.; Visualization, A.J.M.M., D.G.F. and K.M.T.T.; Writing—original draft, A.J.M.M. and D.G.F.; Writing—review and editing, J.A.Z.S. and E.Y.T.C. All authors have read and agreed to the published version of the manuscript.

Funding: This research was funded by the Public Investment Project "Creation of a Geomatics and Remote Sensing Laboratory of the National University Toribio Rodríguez of Mendoza of Amazonas" GEOMATICA, (CUI N° 2255626). The APC was funded by the vice chancellor's office of Research of the National University Toribio Rodriguez of Mendoza of Amazonas.

Data Availability Statement: The data generated for the development of this research are available at the following address: https://code.earthengine.google.com/0811b809ed89944f6750cb197e8e5509 (accessed on 23 July 2023).

Acknowledgments: The authors acknowledge and appreciate the support of the INDES-CES of the National University Toribio Rodríguez of Mendoza of Amazonas (UNTRM).

Conflicts of Interest: The authors declare no conflicts of interest.

References

1. Ni, R.; Tian, J.; Li, X.; Yin, D.; Li, J.; Gong, H.; Zhang, J.; Zhu, L.; Wu, D. An Enhanced Pixel-Based Phenological Feature for Accurate Paddy Rice Mapping with Sentinel-2 Imagery in Google Earth Engine. *ISPRS J. Photogramm. Remote Sens.* **2021**, *178*, 282–296. [CrossRef]
2. Kuenzer, C.; Knauer, K. Remote Sensing of Rice Crop Areas. *Int. J. Remote Sens.* **2013**, *34*, 2101–2139. [CrossRef]
3. Yang, H.; Pan, B.; Wu, W.; Tai, J. Field-Based Rice Classification in Wuhua County through Integration of Multi-Temporal Sentinel-1A and Landsat-8 OLI Data. *Int. J. Appl. Earth Obs. Geoinf.* **2018**, *69*, 226–236. [CrossRef]
4. Phan, H.; Le Toan, T.; Bouvet, A.; Nguyen, L.D.; Duy, T.P.; Zribi, M. Mapping of Rice Varieties and Sowing Date Using X-Band SAR Data. *Sensors* **2018**, *18*, 316. [CrossRef]
5. Nelson, A.; Setiyono, T.; Rala, A.B.; Quicho, E.D.; Raviz, J.V.; Abonete, P.J.; Maunahan, A.A.; Garcia, C.A.; Bhatti, H.Z.M.; Villano, L.S.; et al. Towards an Operational SAR-Based Rice Monitoring System in Asia: Examples from 13 Demonstration Sites across Asia in the RIICE Project. *Remote Sens.* **2014**, *6*, 10773–10812. [CrossRef]
6. You, N.; Dong, J. Examining Earliest Identifiable Timing of Crops Using All Available Sentinel 1/2 Imagery and Google Earth Engine. *ISPRS J. Photogramm. Remote Sens.* **2020**, *161*, 109–123. [CrossRef]
7. de Bem, P.P.; de Carvalho Júnior, O.A.; de Carvalho, O.L.F.; Gomes, R.A.T.; Guimarães, R.F.; Pimentel, C.M.M. Irrigated Rice Crop Identification in Southern Brazil Using Convolutional Neural Networks and Sentinel-1 Time Series. *Remote Sens. Appl. Soc. Environ.* **2021**, *24*, 100627. [CrossRef]
8. Dineshkumar, C.; Kumar, J.S.; Nitheshnirmal, S. Rice Monitoring Using Sentinel-1 Data in the Google Earth Engine Platform. *Multidiscip. Digit. Publ. Inst. Proc.* **2019**, *24*, 4. [CrossRef]
9. Onojeghuo, A.O.; Blackburn, G.A.; Wang, Q.; Atkinson, P.M.; Kindred, D.; Miao, Y. Mapping Paddy Rice Fields by Applying Machine Learning Algorithms to Multi-Temporal Sentinel-1A and Landsat Data. *Int. J. Remote Sens.* **2018**, *39*, 1042–1067. [CrossRef]
10. Rudiyanto; Minasny, B.; Shah, R.M.; Soh, N.C.; Arif, C.; Setiawan, B.I. Automated Near-Real-Time Mapping and Monitoring of Rice Extent, Cropping Patterns, and Growth Stages in Southeast Asia Using Sentinel-1 Time Series on a Google Earth Engine Platform. *Remote Sens.* **2019**, *11*, 1666. [CrossRef]
11. Xiao, W.; Xu, S.; He, T. Mapping Paddy Rice with Sentinel-1/2 and Phenology-, Object-Based Algorithm—A Implementation in Hangjiahu Plain in China Using Gee Platform. *Remote Sens.* **2021**, *13*, 990. [CrossRef]
12. Mosleh, M.K.; Hassan, Q.K.; Chowdhury, E.H. Application of Remote Sensors in Mapping Rice Area and Forecasting Its Production: A Review. *Sensors* **2015**, *15*, 769–791. [CrossRef]
13. Onojeghuo, A.O.; Miao, Y.; Blackburn, G.A. Deep ResU-Net Convolutional Neural Networks Segmentation for Smallholder Paddy Rice Mapping Using Sentinel 1 SAR and Sentinel 2 Optical Imagery. *Remote Sens.* **2023**, *15*, 1517. [CrossRef]
14. Stendardi, L.; Karlsen, S.R.; Niedrist, G.; Gerdol, R.; Zebisch, M.; Rossi, M.; Notarnicola, C. Exploiting Time Series of Sentinel-1 and Sentinel-2 Imagery to Detect Meadow Phenology in Mountain Regions. *Remote Sens.* **2019**, *11*, 542. [CrossRef]
15. Del Pilar García Rodríguez, M.; De Évora, A.S.P. Study of Degraded Areas Throughimages Obtained Froma UAV (Drone) and the ESA Sentinel Satellite. *An. Geogr. La Univ. Complut.* **2020**, *40*, 55–71. [CrossRef]
16. Gorelick, N.; Hancher, M.; Dixon, M.; Ilyushchenko, S.; Thau, D.; Moore, R. Google Earth Engine: Planetary-Scale Geospatial Analysis for Everyone. *Remote Sens. Environ.* **2017**, *202*, 18–27. [CrossRef]
17. White, L.; Brisco, B.; Dabboor, M.; Schmitt, A.; Pratt, A. A Collection of SAR Methodologies for Monitoring Wetlands. *Remote Sens.* **2015**, *7*, 7615–7645. [CrossRef]
18. DeLancey, E.R.; Kariyeva, J.; Cranston, J.; Brisco, B. Monitoring Hydro Temporal Variability in Alberta, Canada with Multi-Temporal Sentinel-1 SAR Data. *Can. J. Remote Sens.* **2018**, *44*, 1–10. [CrossRef]
19. Mutanga, O.; Kumar, L. Google Earth Engine Applications. *Remote Sens.* **2019**, *11*, 591. [CrossRef]
20. Talema, T.; Hailu, B.T. Mapping Rice Crop Using Sentinels (1 SAR and 2 MSI) Images in Tropical Area: A Case Study in Fogera Wereda, Ethiopia. *Remote Sens. Appl. Soc. Environ.* **2020**, *18*, 100290. [CrossRef]

21. Briceño, N.B.R.; Castillo, E.B.; Torres, O.A.G.; Oliva, M.; Tafur, D.L.; Gurbillón, M.Á.B.; Corroto, F.; López, R.S.; Rascón, J. Morphometric Prioritization, Fluvial Classification, and Hydrogeomorphological Quality in High Andean Livestock Micro-Watersheds in Northern Peru. *ISPRS Int. J. Geo-Inf.* **2020**, *9*, 305. [CrossRef]
22. Instituto Nacional de Estadistica e Informatica. Available online: https://m.inei.gob.pe/estadisticas/indice-tematico/poblacion-y-vivienda/ (accessed on 28 September 2023).
23. Castillo, E.B.; Turpo Cayo, E.Y.; De Almeida, C.M.; López, R.S.; Rojas Briceño, N.B.; Silva López, J.O.; Gurbillón, M.Á.B.; Oliva, M.; Espinoza-Villar, R. Monitoring Wildfires in the Northeastern Peruvian Amazon Using Landsat-8 and Sentinel-2 Imagery in the GEE Platform. *ISPRS Int. J. Geo-Inf.* **2020**, *9*, 564. [CrossRef]
24. Souza, C.M.; Shimbo, J.Z.; Rosa, M.R.; Parente, L.L.; Alencar, A.A.; Rudorff, B.F.T.; Hasenack, H.; Matsumoto, M.; Ferreira, L.G.; Souza-Filho, P.W.M.; et al. Reconstructing Three Decades of Land Use and Land Cover Changes in Brazilian Biomes with Landsat Archive and Earth Engine. *Remote Sens.* **2020**, *12*, 2735. [CrossRef]
25. Gómez Fernández, D.; Salas López, R.; Rojas Briceño, N.B.; Silva López, J.O.; Oliva, M. Dynamics of the Burlan and Pomacochas Lakes Using SAR Data in GEE, Machine Learning Classifiers, and Regression Methods. *ISPRS Int. J. Geo-Inf.* **2022**, *11*, 534. [CrossRef]
26. Shelestov, A.; Lavreniuk, M.; Kussul, N.; Novikov, A.; Skakun, S. Exploring Google Earth Engine Platform for Big Data Processing: Classification of Multi-Temporal Satellite Imagery for Crop Mapping. *Front. Earth Sci.* **2017**, *5*, 1–10. [CrossRef]
27. Tsakmakis, I.D.; Gikas, G.D.; Sylaios, G.K. Integration of Sentinel-Derived NDVI to Reduce Uncertainties in the Operational Field Monitoring of Maize. *Agric. Water Manag.* **2021**, *255*, 106998. [CrossRef]
28. Liu, Z.; Chen, Y.; Chen, C. Analysis of the Spatiotemporal Characteristics and Influencing Factors of the NDVI Based on the GEE Cloud Platform and Landsat Images. *Remote Sens.* **2023**, *15*, 4980. [CrossRef]
29. Liu, D.; Chen, N.; Zhang, X.; Wang, C.; Du, W. Annual Large-Scale Urban Land Mapping Based on Landsat Time Series in Google Earth Engine and OpenStreetMap Data: A Case Study in the Middle Yangtze River Basin. *ISPRS J. Photogramm. Remote Sens.* **2020**, *159*, 337–351. [CrossRef]
30. Zurqani, H.A.; Post, C.J.; Mikhailova, E.A.; Schlautman, M.A.; Sharp, J.L. Geospatial Analysis of Land Use Change in the Savannah River Basin Using Google Earth Engine. *Int. J. Appl. Earth Obs. Geoinf.* **2018**, *69*, 175–185. [CrossRef]
31. Du, Y.; Zhang, Y.; Ling, F.; Wang, Q.; Li, W.; Li, X. Water Bodies' Mapping from Sentinel-2 Imagery with Modified Normalized Difference Water Index at 10-m Spatial Resolution Produced by Sharpening the Swir Band. *Remote Sens.* **2016**, *8*, 354. [CrossRef]
32. Feyisa, G.L.; Meilby, H.; Fensholt, R.; Proud, S.R. Automated Water Extraction Index: A New Technique for Surface Water Mapping Using Landsat Imagery. *Remote Sens. Environ.* **2014**, *140*, 23–35. [CrossRef]
33. Gulácsi, A.; Kovács, F. Sentinel-1-Imagery-Based High-Resolution Water Cover Detection on Wetlands, Aided by Google Earth Engine. *Remote Sens.* **2020**, *12*, 1614. [CrossRef]
34. Zhang, M.; Chen, F.; Tian, B. An Automated Method for Glacial Lake Mapping in High Mountain Asia Using Landsat 8 Imagery. *J. Mt. Sci.* **2018**, *15*, 13–24. [CrossRef]
35. Nafarin, N.A.; Novitasari, N. Relationship between Normalized Difference Vegetation Index (NDVI) and Rice Growth Phases in Danda Jaya Swamp Irrigation Area Regency Barito Kuala. *IOP Conf. Ser. Earth Environ. Sci.* **2023**, *1184*, 012019. [CrossRef]
36. Cui, J.; Guo, Y.; Xu, Q.; Li, D.; Chen, W.; Shi, L.; Ji, G. Extraction of Information on the Flooding Extent of Agricultural Land in Henan Province Based on Multi-Source Remote Sensing Images and Google Earth Engine. *Agronomy* **2023**, *13*, 355. [CrossRef]
37. Lindsay, E.; Frauenfelder, R.; Ruther, D.; Nava, L.; Rubensdotter, L.; Strout, J.; Nordal, S. Multi-Temporal Satellite Image Composites in Google Earth Engine for Improved Landslide Visibility: A Case Study of a Glacial Landscape. *Remote Sens.* **2022**, *14*, 2301. [CrossRef]
38. Zeng, J.; Tan, M.L.; Tew, Y.L.; Zhang, F.; Wang, T.; Samat, N.; Tangang, F.; Yusop, Z. Optimization of Open-Access Optical and Radar Satellite Data in Google Earth Engine for Oil Palm Mapping in the Muda River Basin, Malaysia. *Agriculture* **2022**, *12*, 1435. [CrossRef]
39. Breiman, L.E.O. Random Forests. *Mach. Learn.* **2001**, *45*, 5–32. [CrossRef]
40. Wang, X.; Fang, S.; Yang, Y.; Du, J.; Wu, H. A New Method for Crop Type Mapping at the Regional Scale Using Multi-Source and Multi-Temporal Sentinel Imagery. *Remote Sens.* **2023**, *15*, 2466. [CrossRef]
41. Romero, M. Comparación de Medias En Grupos Apareados o Dependientes. *Enfermería Trab.* **2013**, *3*, 118–123.
42. Vizzari, M. PlanetScope, Sentinel-2, and Sentinel-1 Data Integration for Object-Based Land Cover Classification in Google Earth Engine. *Remote Sens.* **2022**, *14*, 2628. [CrossRef]
43. Wu, J.; Jin, S.; Zhu, G.; Guo, J. Monitoring of Cropland Abandonment Based on Long Time Series Remote Sensing Data: A Case Study of Fujian Province, China. *Agronomy* **2023**, *13*, 1585. [CrossRef]
44. Singha, C.; Swain, K.C. Rice Crop Growth Monitoring with Sentinel 1 SAR Data Using Machine Learning Models in Google Earth Engine Cloud. *Remote Sens. Appl. Soc. Environ.* **2023**, *32*, 101029. [CrossRef]
45. da Costa Freitas, C.; de Souza Soler, L.; Sant'Anna, S.J.S.; Dutra, L.V.; Dos Santos, J.R.; Mura, J.C.; Correia, A.H. Land Use and Land Cover Mapping in the Brazilian Amazon Using Polarimetric Airborne P-Band SAR Data. *IEEE Trans. Geosci. Remote Sens.* **2008**, *46*, 2956–2970. [CrossRef]
46. DeVries, B.; Huang, C.; Armston, J.; Huang, W.; Jones, J.W.; Lang, M.W. Rapid and Robust Monitoring of Flood Events Using Sentinel-1 and Landsat Data on the Google Earth Engine. *Remote Sens. Environ.* **2020**, *240*, 111664. [CrossRef]

47. Xue, H.; Xu, X.; Zhu, Q.; Yang, G.; Long, H.; Li, H.; Yang, X.; Zhang, J.; Yang, Y.; Xu, S.; et al. Object-Oriented Crop Classification Using Time Series Sentinel Images from Google Earth Engine. *Remote Sens.* **2023**, *15*, 1353. [CrossRef]
48. Tian, F.; Wu, B.; Zeng, H.; Zhang, X.; Xu, J. Efficient Identification of Corn Cultivation Area with Multitemporal Synthetic Aperture Radar and Optical Images in the Google Earth Engine Cloud Platform. *Remote Sens.* **2019**, *11*, 629. [CrossRef]
49. De Alban, J.D.T.; Connette, G.M.; Oswald, P.; Webb, E.L. Combined Landsat and L-Band SAR Data Improves Land Cover Classification and Change Detection in Dynamic Tropical Landscapes. *Remote Sens.* **2018**, *10*, 306. [CrossRef]
50. Saad El Imanni, H.; El Harti, A.; Hssaisoune, M.; Velastegui-Montoya, A.; Elbouzidi, A.; Addi, M.; El Iysaouy, L.; El Hachimi, J. Rapid and Automated Approach for Early Crop Mapping Using Sentinel-1 and Sentinel-2 on Google Earth Engine; A Case of a Highly Heterogeneous and Fragmented Agricultural Region. *J. Imaging* **2022**, *8*, 316. [CrossRef]